Proceedings of the Combustion Institute 40 (2024) 105357

Contents lists available at ScienceDirect

Proceedings of the Combustion Institute

journal homepage: www.elsevier.com/locate/proci

Development of fully fiber-coupled phosphor thermometry imaging for combustion applications

Patrick Nau *, Hannah Scheffold, Niklas Petry, Zhiyao Yin

German Aerospace Center (DLR), Institute of Combustion Technology, Pfaffenwaldring 38–40, 70569 Stuttgart, Germany

ARTICLE INFO

Keywords:
Phosphor thermometry
Hydrogen combustion
Wall temperature
Gas turbine
Fiber

ABSTRACT

Fully fiber-coupled phosphor thermometry imaging was demonstrated in an atmospheric fuel-flexible jet-stabilized combustor operated with methane–hydrogen–air flames. Different fuel-air mixedness and operating conditions ranging from 100% methane to 100% hydrogen were investigated. The phosphor $GdAlO_3$:Cr was excited at 532 nm using a fiber bundle, while an imaging fiber bundle was used for signal detection. The presented setup allowed to cover a temperature range from 400–1100 °C with a precision of 0.2–2%. Temperature maps of the combustor walls for six operating conditions will be presented and the influence of the different flame conditions on the wall temperatures will be discussed.

1. Introduction

The utilization of hydrogen combustion in gas turbines plays a pivotal role in the ongoing shift toward sustainable power production [1]. It complements renewable electricity generation and is essential to address the intermittency of power production from sources such as wind and solar power. To achieve a reliable and flexible power supply, the integration of hydrogen as a fuel source in gas turbines presents a promising solution. Hydrogen combustion stands out for its environmentally friendly characteristics, producing only water as its primary byproduct and avoiding carbon dioxide emissions that contribute to greenhouse gases. Furthermore, hydrogen can be generated through various methods, including renewable sources like solar and wind power, facilitating a closed-loop energy system where sustainable resources power the hydrogen production. This hydrogen can then be stored, transported, and strategically utilized in gas turbines to release power as needed.

Especially during the transitional phase from fossil fuels to sustainable alternatives, gas turbines will operate using various fuels or fuel mixtures. Given the substantial differences in combustion properties among these fuels, the development of gas turbines with fuel-flexible burner designs is imperative [2]. An integral aspect of this development is the precise knowledge of wall temperatures within gas turbine combustors, as these temperatures directly influence turbine efficiency and performance. Elevated wall temperatures may lead to material deterioration and reduced engine lifespan, whereas lower wall temperatures can result in suboptimal combustion and decreased engine performance. The accurate measurement and control of wall temperatures are, therefore, critical for optimizing gas turbine combustor performance and ensuring safe and efficient operation.

Phosphor thermometry has demonstrated its remarkable capability to deliver precise and accurate temperature measurements in this context, as evidenced by prior studies [3–6]. This method relies on the use of luminescent particles that are stimulated by a light source, typically a laser. Subsequently, the emitted light is meticulously analyzed to derive temperature data, leveraging either the phosphorescence lifetime or the emission spectrum. While the emission spectrum is in most cases utilized by taking the intensity ratio of two emission lines, also the complete spectrum can be evaluated to measure temperatures [7]. The lifetime is usually measured by fitting the phosphorescence intensity decay curve or taking the intensity ratio at two positions in time after excitation. Also the phase angle in the frequency domain can be utilized [4,8]. While most applications measure the temperature online, thermographic phosphors can also measure temperatures offline. In this case the irreversible change of the luminescent properties after exposure to high temperatures is analyzed to obtain the maximum temperature exposed to the object under investigation, like gas turbine combustor walls [9]. This approach does not require optical access to the investigated object during the experiment and can be beneficial in certain applications. Besides high temperature processes, phosphor thermometry can also be used for in vivo temperature measurements [10] or harsh environments like nuclear waste storage [11]. By seeding luminescent particles in a gas or liquid flow, a combination of thermometry and flow field measurements can be achieved [12].

* Corresponding author.
E-mail address: patrick.nau@dlr.de (P. Nau).

https://doi.org/10.1016/j.proci.2024.105357
Received 30 November 2023; Accepted 11 June 2024
Available online 29 June 2024

By volumetric illumination even a simultaneous 3D temperature and velocity measurement can be realized [13].

However, conducting optical measurements can be a challenge in the context of large-scale test rigs with dimensions and operational conditions resembling those of real engines. This limitation is mainly due to restricted optical access. In such scenarios, a practical solution frequently involves employing a fiber-coupled configuration. In fact, fiber-coupled phosphor thermometry has already been successfully implemented in gas turbine combustors, with notable applications including temperature measurements on stator vanes [14,15] and the walls of large-scale gas turbine combustors [16].

To maximize the information gathered during a measurement campaign an imaging technique would be desirable. Therefore, fully fiber-coupled phosphor thermometry imaging was developed and tested in a lab experiment and the results are being presented here. Different approaches can be used to measure temperatures with phosphor thermometry [5,8]. The most common are the intensity-ratio method and the lifetime method and these will be briefly discussed here. The intensity-ratio method uses the temperature dependence of the intensity-ratio of different emission lines of the phosphor. This approach can be implemented as a 2D-technique by using two cameras with different band-pass filters. The images of both cameras must be overlapped carefully. Then the ratio of both images will be calculated for each pixel and the temperature obtained from a proper calibration. The drawback of this approach is that it is prone to systematic errors. If the images are not overlapped properly or the alignment of the cameras changes during the experiment, i.e. due to vibrations, wrong pixel values will be used resulting in an error in the temperature. Also signal attenuation due to beam steering, window contamination or signal absorption can be different for both cameras because they are detecting light in a different spectral region. These effects can also cause systematic errors. While a correction in a lab environment is often possible, it is very difficult for a real gas turbine application. Once the optical probe has been installed in the test rig it is difficult to access it to perform additional calibration measurements. Furthermore, the intensity ratio method is usually less sensitive than the lifetime method especially for the temperatures present in a gas turbine [4].

We decided therefore to use the lifetime method. In this approach, the temperature dependence of the phosphorescence decay time τ is used. The sensitivity is very high and systematic errors are minimal. Because the signal is detected in the time domain, the absolute intensity of the signal does not affect the measured temperature. Decay times of thermographic phosphors are usually in a range between milliseconds down to microseconds or nanoseconds. To measure the decay time several options are possible. The most common ones will be discussed briefly. A double frame camera captures one image with a short gate followed by a second frame with a long gate. The ratio of both frames can be used to obtain the decay time. Because only two frames are used, the accuracy is limited and the dynamic range can be reduced [17]. With an intensified gated camera, the gate of the camera can be adjusted in duration and position in the nanosecond range. Therefore, even very short decay times below microseconds can be resolved. The position of the gate can be shifted from one image to the next and the full decay curve is resolved using multiple images [18]. Because only one image can be captured for each laser shot, the images from several laser shots must be captured. This, however, has the drawback that the measurement time will become very long and this approach is only useful for steady state applications. An alternative is the utilization of high-speed cameras. The detection scheme is similar to photomultiplier tubes (PMTs). The phosphor is excited with a laser pulse and the phosphorescence decay detected with the high-speed camera. With frame rates of several hundred kHz, decay times of a few microseconds can be measured.

Table 1
Operating conditions of all investigated flames, with mass flow rate Q for CH_4, H_2 and air, calculated adiabatic flame temperature T_{ad} and measured exhaust gas temperature T_{ex}. The global equivalence ratio for all flames was $\Phi = 0.74$.

Mixing	H_2 fuel content [vol%]	$Q(CH_4)$ [g/s]	$Q(H_2)$ [g/s]	Q(Air) [g/s]	P_{th} [kW]	T_{ad} [K]	T_{ex} [K]
Premixed	0	0.20	0	4.65	10	2096	1291
Premixed	50	0.15	0.02	4.50	10	2126	1277
Premixed	100	0	0.083	3.85	10	2271	1318
Non-premixed	0	0.20	0	4.65	10	2096	1301
Non-premixed	50	0.15	0.02	4.50	10	2126	1300
Non-premixed	100	0	0.083	3.85	10	2271	1354

2. Experimental

2.1. Model combustor and operating conditions

A detailed description of the combustor and operating conditions can be found at Petry et al. [19]. The combustor is schematically illustrated in Fig. 1. The top view in Fig. 1b shows the rectangular cross section (40 × 50 mm) of the combustor. The off-centered position of the jet ensured the formation of a pronounced recirculation zone on one side of the combustion chamber. Two nozzle configurations were investigated as shown in the side views in Fig. 1c and d. The air nozzle had an inner diameter of D=10 mm and the fuel nozzle (inner diameter 1.5 mm) was centered in this nozzle. The distance between air nozzle exit and burner baseplate was 20 mm and the fuel nozzle exit was either flush with the air nozzle (non-premixed configuration Fig. 1c) or located 50 mm upstream of the air nozzle (technically premixed configuration Fig. 1d). The combustion chamber consisted of two segments (Fig. 1a) with quartz walls on all four sides (thickness 8 mm) compressed by water cooled posts. The height of each segment was 200 mm.

The investigated operating conditions are summarized in Table 1. All cases had a global equivalence ratio of $\Phi = 0.74$ and a thermal power of 10 kW. The air nozzle exit velocity was 110 m/s. Air was preheated to 573 K measured in the air plenum. All experiments were conducted at atmospheric pressure. The fuel was either methane, hydrogen or a mixture of 50 vol% methane and 50 vol% hydrogen.

2.2. Optical measurement setup

A schematic of the optical setup is shown in Fig. 1. We decided to use separate fibers for excitation and detection to avoid possible damage to the imaging fiber bundle from the laser beam. Excitation of the phosphor was accomplished with a Nd:YAG Laser (Innolas, Spitlight 600, 532 nm, 15 Hz, 6 ns pulse length). The laser beam was coupled in a fiber bundle of 14 fibers (Thorlabs, FG910UEC, NA = 0.22, 910 µm core diameter, 3 m long). Coupling was achieved with a collimating lens (f = +100 mm) with the laser focus in front of the fibers. After the focus the beam expanded to the size of the fiber bundle. Due to the air gaps between the individual fibers the achieved coupling efficiency was limited to about 40%. To avoid hot-spots in the laser beam profile, that can cause fiber damage, and to achieve a homogeneous illumination of the individual fibers, the laser resonator was changed to a stable resonator design with a near flat-top beam profile. The resulting high M^2 of about 20 prevents optical breakdown in the focus of the coupling lens. The beams exiting the fibers were recollimated (f = +25 mm) and imaged on an area of about 55 × 55 mm^2. To achieve a more homogeneous illumination the recollimation optics were slightly defocused. The total laser energy on this area was about 10 mJ. The illuminated area was imaged with a second lens (f = +35 mm) on an imaging fiber bundle (Nanjing, 40000 px, 5 × 5 mm). A bandpass filter (LOT, 650FSX40-50) limited the detected light to 650 nm with a bandwidth of 50 nm. The light was then guided with the fiber bundle to the high-speed camera (Phantom v1212, up to 500 kHz frame rate with 256 × 32 px). To be

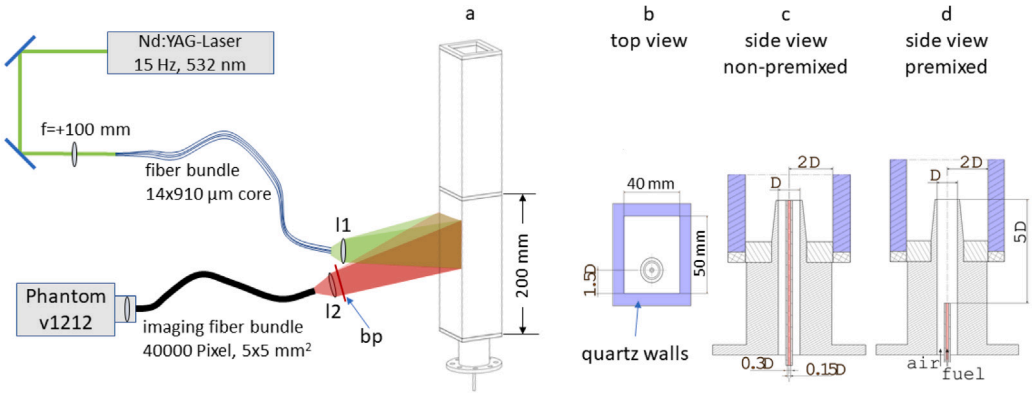

Fig. 1. a: Schematic of the experimental setup. The laser beam was coupled in a fiber bundle (14 × 910 µm core diameter) and recollimated with lens l1 (f = +25 mm) on the combustor window. Phosphorescence was coupled into an imaging fiber bundle with lens l2 (f = +35 mm) behind a band pass filter (bp). b: Top view of the combustor. The air nozzle inner diameter was D = 10 mm. c: Side view in non-premixed nozzle configuration. d: Side view in technically premixed configuration.

able to use a frame rate of up to 500 kHz only 256 × 32 px of the camera chip were used. The end face of the fiber bundle was imaged on the camera chip with another lens (f = +12 mm). Due to the square shape of the fiber end face, effectively only 32 × 32 px of the camera chip were used. This resulted in a pixel size of 1.7 mm/px. This resolution was still sufficient for the application. The pixel size in the object plane was measured with a chequered pattern target. A correction for image distortion was not necessary.

The phosphor selected for this investigation was $GdAlO_3$:Cr (Phosphor Technology). This phosphor can be excited very efficiently at 532 nm and covers a relatively broad temperature range (about 400 – 1100 °C) [20]. This is ideal for the intended application with relatively cold walls near the nozzle and high temperatures further downstream. The phosphor was spray-painted on the quartz walls of a jet-stabilized model combustor using the commercial HPC binder of Zyp Coatings. We applied thin phosphor coatings to the windows by using an airbrush (Badger 100). To ensure uniformity, multiple layers were spray-painted and subsequently dried using a heat gun. A mixing ratio of 2 g phosphor powder in 10 mL binder was used. This coating procedure has been used successfully for similar experiments in our lab before [21]. Our target thickness for these coatings was approximately 20 µm, a value known to minimize errors resulting from thermal gradients. This has been investigated numerically for gas turbine applications [22] and experimentally in an car engine [23]. In the experimental investigation no temperature difference was found between excitation from the front and back side of the coating for a thickness ≤20 µm. We estimate that the error due to temperature gradients in the coating is below the measurement accuracy. Given the challenge of directly measuring thickness on the quartz wall, we coated small steel samples with the same coating process, and their thickness was quantified using a coating thickness gauge (Sauter, TE 1250-0.1FN). For Calibration measurements one of the coated windows was placed in an optically accessible furnace (LAC, VP 10/16, Boldt Wärmetechnik GmbH) with a thermocouple (type B) placed on the opposite side of the coated window. Due to the limited optical access to the oven, in this case an area of about 10 × 10 mm^2 was illuminated with the same laser energy density as in the combustor measurements. The front imaging optics was adapted to image these 10 × 10 mm^2 on the imaging-fiber end-face while the imaging optics on the camera chip remained unchanged.

3. Results and discussion

3.1. Data evaluation and calibration

For each laser shot, a series of 1000 images was captured and at each measurement condition 150 laser shots were measured. The images of the individual laser shots were averaged to obtain a series of 1000 images averaged over 150 laser shots. For each pixel, a time series of the signal intensity was created as shown exemplarily in Fig. 2(a). Image acquisition was started 1 ms before the laser pulse to capture background intensity. The signal intensity depends on the integration time, resulting in five times higher signal for the 100 kHz data compared to 500 kHz. It was observed that the background level was actually not constant but has an exponentially decaying shape. This is an artifact caused by the measurement mode used to synchronize camera and laser. The decay rate of this offset was very similar for all measurement conditions and camera frame rates. However, the rise-time of the background depends on the frame rate of the camera. To correct for this a mono-exponential curve was fitted to the background and subtracted from the data (Fig. 2(b)). Further calibration measurements or image correction procedures like a flat field correction were not necessary with this procedure.

After background subtraction the decay time was obtained with a non-linear least-squares fit of a mono-exponential curve. Because the phosphorescence decay curve is not mono-exponential, the obtained decay time τ depends on the fitting-window, which is the region of the curve that is used for fitting. Two main methods to determine the fitting-window are established. The iterative approach defines start and end position as a multiple of τ ($t_{start} = c_1 \times \tau$ and $t_{stop} = c_2 \times \tau$). Because the fitting window depends on τ and the resulting τ depends again on the fitting window, the fit was performed iteratively until it converges. We used $c_1 = 0.5$ and $c_2 = 3$ in this investigation. This fit is referred to as the "late fit" in the following. The second method is an intensity based approach using a threshold relative to the peak intensity. This definition can be problematic, when the curve has a pronounced multi-exponential shape with an intense short spike at the beginning. For $GdAlO_3$:Cr this is the case for cold temperatures. We used this approach therefore for $T > 800$ °C, beginning right at the peak and stopping the fit when the intensity drops below 5% of the peak intensity ("early fit").

The decay times τ obtained for all pixels during calibration are shown exemplarily at 750 °C in Fig. 3(a). For the 100 kHz data the late fit was used (top) and for 500 kHz the early fitting window (bottom). As can be seen, the early fit results in lower values for τ as expected. It is also visible, that the map of decay times is not flat. In the top right corner systematically higher values for τ are obtained. We made sure that this is not caused by a temperature gradient or inhomogeneities of the laser beam. It is caused by the individual non-linear characteristics of the camera pixels. This behavior is well known for this type of cameras [24,25].

Instead of performing an additional calibration of the non-linearities [26], we used a single step calibration procedure, by measuring the decay time τ at different temperatures for each pixel. A similar approach has already been used before [27]. To avoid systematic errors the same optical setup, laser fluence and similar signal intensities were

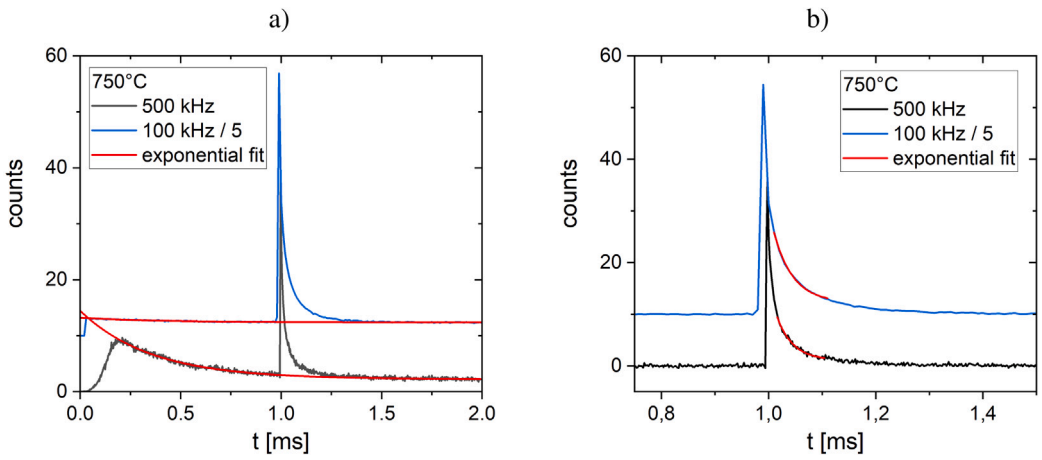

Fig. 2. Time traces of the signal intensity measured in an oven at 750 °C for one camera pixel at 500 kHz and 100 kHz. An Exponential curve is fitted to the background (a) and subtracted from the data to obtain background corrected data (b). The blue curve (100 kHz) was shifted for clarity. (For interpretation of the references to color in this figure legend, the reader is referred to the web version of this article.)

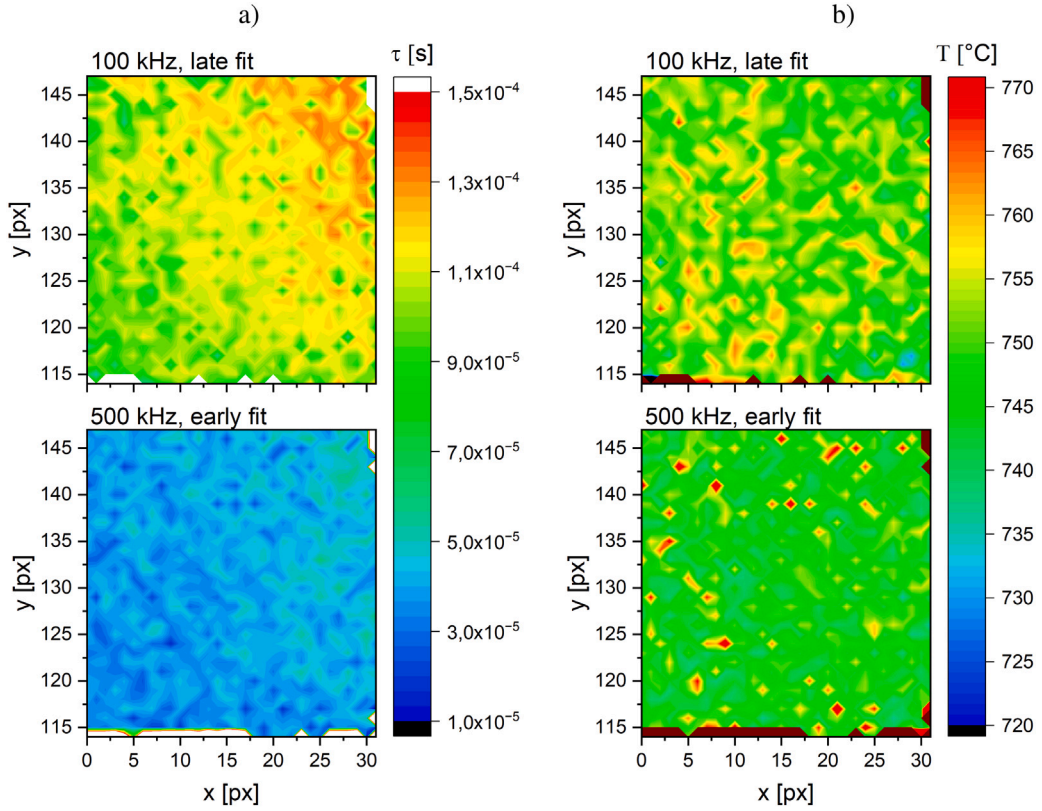

Fig. 3. Results from the calibration measurements at 750 °C. (a): Decay times at 100 kHz (top) and 500 kHz (bottom). (b): Temperatures at 100 kHz (top) and 500 kHz (bottom) after calibration.

used during calibration and flame measurements. The calibration data is shown exemplarily for pixel $x = 15$ and $y = 135$ in Fig. 4(a). A second order polynomial was used to interpolate the calibration data. This polynomial was later used to calculate temperatures from measured decay times. In Fig. 3(b) the resulting temperature map after applying the calibration to the decay times in Fig. 3(a) is shown. The temperature maps are now flat without systematic bias due to pixel non-linearities. Some random pixels with higher temperatures can still be seen especially in the 500 kHz data. This is caused by the non-iterative fitting algorithm with an early fitting window which is more vulnerable to such outliers. For data evaluation of the flame measurements at this temperature the results from the "late fit" using the 100 kHz data were used.

From the resulting 2D maps the standard deviation of all pixels were calculated. The resulting values between 2–12 K or 0.2–2% are shown in Fig. 4(b). Not a single combination of camera frame rate and fitting window was suitable to cover the complete temperature range. At short decay times a higher frame rate is necessary to resolve the decay curve. At lower temperatures it is however desirable to use a lower frame rate to benefit from the higher signal level and resulting lower standard deviation. While the late fit fails at high temperatures, because not enough data points are available, the early fit fails at low temperatures, because the peak of the curve is dominated by a strong

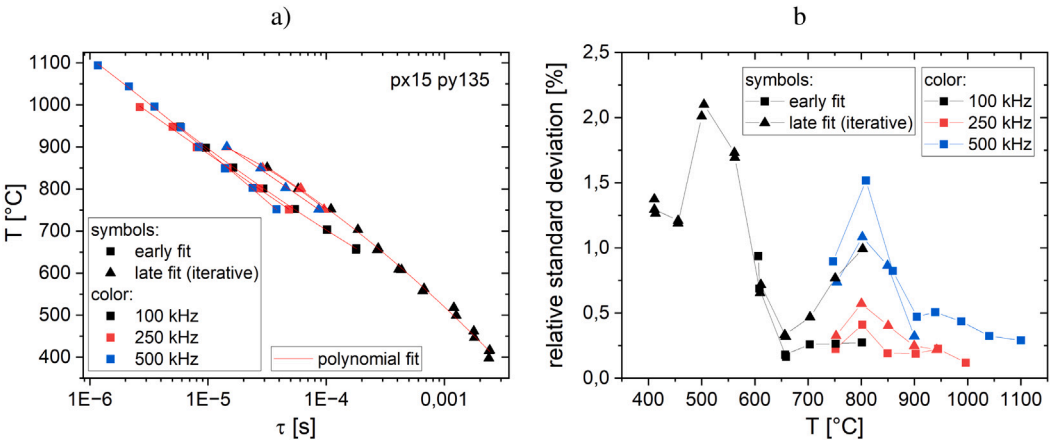

Fig. 4. Calibration data for pixel $x = 15$ and $y = 135$ for all used frame rates and fitting windows (a) and relative standard deviation of all pixels (b).

spike. Therefore we used preferably the late fit at 100 kHz for low temperatures and the early fit at 500 kHz and switched dynamically for each pixel between the data evaluation strategies and data from different measurement modes during post-processing, depending on the temperature at the given pixel. The total measurement accuracy depends mainly on the precision of the obtained decay rates as described above, and errors from the calibration procedure like the accuracy of the reference temperature measurement in the oven. These errors were estimated to about 0.5–0.7% resulting in a total measurement accuracy of 6–14 K.

3.2. Wall temperature measurements

Wall temperatures measured on three windows measured for six investigated flame conditions are shown in Fig. 5. The temperature maps were constructed by overlapping four measurements at different heights. No interpolation was used in the overlapping regions (around z = 50, 100 and 150 mm). In general, the agreement of the temperatures in the overlapping regions is very good, showing the good accuracy and reliability of the measurement system and data evaluation procedures. Missing values are visible for temperatures below 400 °C in the lower area of the windows and for temperatures above 1100 °C. For the non-premixed case unfortunately only measurements at 100 kHz were available for z < 105 mm. Therefore some additional missing values are present in this region.

Window c is located close to the air-fuel-jet, while side a is located opposite to the jet and window b is on the wide side of the combustion chamber. Flow field, flame position, adiabatic flame temperatures and exhaust gas temperatures have recently been analyzed for these flames [19]. An increase of the hydrogen content results in shorter lift-off-height (LOH), due to the higher flame speed. In addition, the LOH in the technically premixed flames is shorter, when compared to the non-premixed conditions. This effect is more pronounced in the 100% hydrogen flames. The different flame positions are also visible in the wall temperatures on wall c, which is close to the jet. In contrast, the shape of the temperature map on side a is only slightly influenced. This is because wall a is mainly affected by the recirculated exhaust gas of the flame, while the flow field is very similar for all flames. The off-centered position of the jet is to some extent also visible on side b.

The measured exhaust gas temperatures and calculated adiabatic flame temperatures are very similar for the 100% methane and 50 vol% cases, but significantly higher in the 100% hydrogen cases (compare Table 1). This is also reflected in the peak temperatures on the walls. Because the methane flame extends also into the second combustor segment, the peak temperature is not captured on side c with the measurements shown in Fig. 5. The temperature drop downstream is caused by the water cooled metal frame of the two combustor segments.

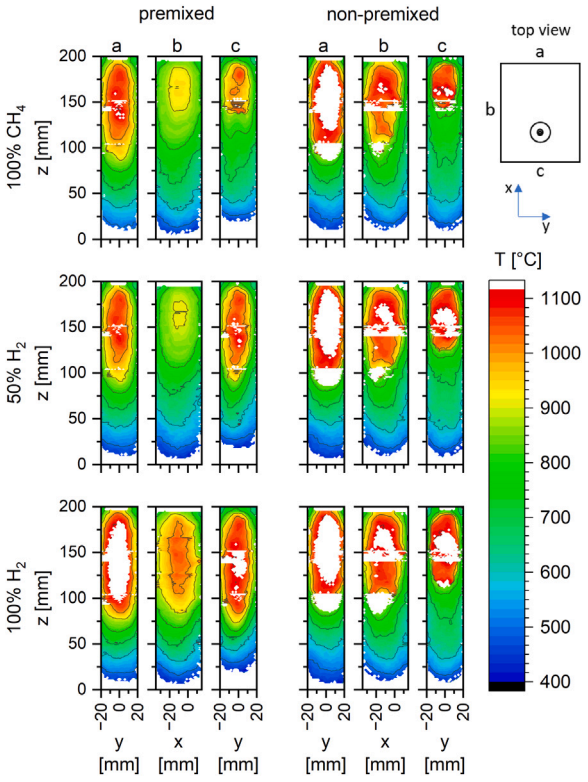

Fig. 5. Temperatures for all investigated flame conditions ranging from 100% CH_4 (top row) to 100% H_2 (bottom row) using technically premixed fuel-air-mixtures (left) and non-premixed conditions (right) on windows a, b and c. The nozzle is located at $x = y = 0$ mm and the baseplate at $z = 0$ mm. Missing values are shown white.

Due to the higher gas temperatures in the non-premixed conditions and for the premixed 100% hydrogen case, the peak temperature could not be resolved with the used setup. A different phosphor or a camera with a much higher frame rate would be necessary.

4. Conclusion

In this investigation we showed that fiber-coupled phosphor thermometry imaging can be applied to the conditions in a gas turbine combustor. Here we covered a temperature range of 400–1100 °C using $GdAlO_3$:Cr. This allowed to cover almost the complete temperature range on the combustor wall. For higher temperatures a different phosphor or a camera with higher frame rates than 500 kHz are necessary.

The used laser energy of 10 mJ was sufficient to measure an area of 55 × 55 mm^2 with a pixel size of 1.7 mm/px. The laser energy was low enough that excitation with a single large core fiber instead of a fiber bundle would be possible. For laser coupling into a single large-core (910 µm) optical fiber we could achieve a coupling efficiency of up to 90% and more than 10 mJ transmitted laser energy down to laser wavelengths of 355 nm. The obtained temperature maps further support previously measured flame positions, flow field and exhaust gas temperatures and will be used to validate and improve numerical simulations.

Novelty and Significance Statement

To the authors' knowledge, this is the first demonstration of fully fiber-coupled phosphor thermometry imaging for use in gas turbine combustors, extending previous work with point measurements in technical conditions. 2D temperature maps were measured on the walls of a model combustor fueled with methane and hydrogen. This is a significant contribution as it enables the application of this technique under technically relevant conditions.

CRediT authorship contribution statement

Patrick Nau: Performed research, Analyzed data, Wrote paper. **Hannah Scheffold:** Analyzed data. **Niklas Petry:** Operated experiment. **Zhiyao Yin:** Set up experiment.

Declaration of competing interest

The authors declare that they have no known competing financial interests or personal relationships that could have appeared to influence the work reported in this paper.

Acknowledgments

This project has received funding from the European Union's Horizon 2020 research and innovation programme under grant agreement No 884229.

References

[1] S. Öberg, M. Odenberger, F. Johnsson, Exploring the competitiveness of hydrogen-fueled gas turbines in future energy systems, Int. J. Hydrog. Energy 47 (1) (2022) 624–644, http://dx.doi.org/10.1016/j.ijhydene.2021.10.035.

[2] M. Huth, A. Heilos, 14 - Fuel flexibility in gas turbine systems: Impact on burner design and performance, in: P. Jansohn (Ed.), Modern Gas Turbine Systems, Woodhead Publishing, 2013, pp. 635–684, http://dx.doi.org/10.1533/9780857096067.3.635.

[3] S.W. Allison, G.T. Gillies, Remote thermometry with thermographic phosphors: Instrumentation and applications, Rev. Sci. Instrum. 68 (7) (1997) 2615–2650, http://dx.doi.org/10.1063/1.1148174.

[4] M. Aldén, A. Omrane, M. Richter, G. Särner, Thermographic phosphors for thermometry: A survey of combustion applications, Prog. Energ. Comb. Sci. 37 (4) (2011) 422–461, http://dx.doi.org/10.1016/j.pecs.2010.07.001.

[5] J. Brübach, C. Pflitsch, A. Dreizler, B. Atakan, On surface temperature measurements with thermographic phosphors: A review, Prog. Energ. Comb. Sci. 39 (1) (2013) 37–60, http://dx.doi.org/10.1016/j.pecs.2012.06.001.

[6] S.W. Allison, A brief history of phosphor thermometry, Meas. Sci. Technol. 30 (7) (2019) 072001, http://dx.doi.org/10.1088/1361-6501/ab1d02.

[7] V. Lechner, C. Betrancourt, C. Mirat, P. Scouflaire, S. Ducruix, Full spectrum fitting method: A new approach for instantaneous phosphor thermometry in harsh environments, Exp. Fluids 63 (7) (2022) 110, http://dx.doi.org/10.1007/s00348-022-03461-2.

[8] M.D. Dramićanin, Trends in luminescence thermometry, J. Appl. Phys. 128 (4) (2020) 040902, http://dx.doi.org/10.1063/5.0014825.

[9] S. Araguás Rodríguez, T. Jelínek, J. Michálek, Á. Yáñez-González, F. Schulte, C.C. Pilgrim, J.P. Feist, S.J. Skinner, Accelerated thermal profiling of gas turbine components using luminescent thermal history paints, in: Proceedings of the 1st Global Power and Propulsion Forum, GPPF 2017, Zurich, Switzerland, 2017-01-16/2017-01-18.

[10] Y. Wu, F. Li, Y. Wu, H. Wang, L. Gu, J. Zhang, Y. Qi, L. Meng, N. Kong, Y. Chai, Q. Hu, Z. Xing, W. Ren, F. Li, X. Zhu, Lanthanide luminescence nanothermometer with working wavelength beyond 1500 nm for cerebrovascular temperature imaging in vivo, Nature Commun. 15 (1) (2024) 2341, http://dx.doi.org/10.1038/s41467-024-46727-5.

[11] A. Sposito, E. Heaps, G. Sutton, G. Machin, R. Bernard, S. Clarke, Phosphor thermometry for nuclear decommissioning and waste storage, Nucl. Eng. Des. 375 (2021) 111091, http://dx.doi.org/10.1016/j.nucengdes.2021.111091.

[12] C. Abram, B. Fond, F. Beyrau, Temperature measurement techniques for gas and liquid flows using thermographic phosphor tracer particles, Prog. Energ. Comb. Sci. (2017) http://dx.doi.org/10.1016/j.pecs.2017.09.001.

[13] M. Stelter, F. Martins, F. Beyrau, B. Fond, Thermographic 3D particle tracking velocimetry for turbulent gas flows, Meas. Sci. Technol. 34 (7) (2023) http://dx.doi.org/10.1088/1361-6501/acc600.

[14] B.W. Noel, H.M. Borella, W. Lewis, W.D. Turley, D.L. Beshears, G.J. Capps, M.R. Cates, J.D. Muhs, K.W. Tobin, Evaluating thermographic phosphors in an operating turbine engine, J. Eng. Gas Turbines Power 113 (2) (1991) 242–245, http://dx.doi.org/10.1115/1.2906554.

[15] J.I. Eldridge, S.W. Allison, T.P. Jenkins, S.L. Gollub, C.A. Hall, D.G. Walker, Surface temperature measurements from a stator vane doublet in a turbine afterburner flame using a YAG:Tm thermographic phosphor, Meas. Sci. Technol. 27 (12) (2016) 125205, http://dx.doi.org/10.1088/0957-0233/27/12/125205.

[16] P. Nau, A. Müller, N. Petry, S. Nilsson, T. Endres, M. Richter, B. Witzel, Fiber-coupled phosphor thermometry for wall temperature measurements in a full-scale hydrogen gas turbine combustor, Meas. Sci. Technol. 34 (10) (2023) 104003, http://dx.doi.org/10.1088/1361-6501/ace542.

[17] B. Heeg, J. Eldridge, T. Jenkins, Precision and accuracy considerations for phosphorescence lifetime thermometry imaging using rapid lifetime determination, in: Proceedings of the International Instrumentation Symposium, 2014.

[18] J. Eldridge, A.C. Wroblewski, D.E. Wolfe, Temperature Mapping at the Thermal Barrier Coating/Bond Coat Interface by Luminescence Lifetime Imaging Using Integrated Erbium-Doped Sublayers, Tech. Rep. GRC-E-DAA-TN64850, 2019.

[19] N. Petry, M. Mannazhi, Z. Yin, O. Lammel, K.P. Geigle, A. Huber, Investigation of fuel and load flexibility of an atmospheric single nozzle jet-stabilized FLOX® combustor with hydrogen/methane-air mixtures, J. Eng. Gas Turb. Power 146 (2023) GTP–23–1439, http://dx.doi.org/10.1115/1.4063782.

[20] J.I. Eldridge, M.D. Chambers, Temperature sensing above 1000 °C using Cr-doped GdAlO3 spin-allowed broadband luminescence, AIP Conf. Proc. 1552 (1) (2013) 873–878, http://dx.doi.org/10.1063/1.4819659.

[21] P. Nau, Z. Yin, O. Lammel, W. Meier, Wall temperature measurements in gas turbine combustors with thermographic phosphors, J. Eng. Gas Turb. Power 141 (4) (2018) 041021, http://dx.doi.org/10.1115/1.4040716.

[22] C.C. Pilgrim, J.P. Feist, A.L. Heyes, On the effect of temperature gradients and coating translucence on the accuracy of phosphor thermometry, Meas. Sci. Technol. 24 (10) (2013) 105201, http://dx.doi.org/10.1088/0957-0233/24/10/105201.

[23] C. Knappe, M. Algotsson, P. Andersson, M. Richter, M. Tunér, B. Johansson, M. Aldén, Thickness dependent variations in surface phosphor thermometry during transient combustion in an HCCI engine, Combust. Flame 160 (8) (2013) 1466–1475, http://dx.doi.org/10.1016/j.combustflame.2013.02.023.

[24] V. Weber, J. Brübach, R.L. Gordon, A. Dreizler, Pixel-based characterisation of CMOS high-speed camera systems, Appl. Phys. B 103 (2) (2011) 421–433, http://dx.doi.org/10.1007/s00340-011-4443-1.

[25] R. Hain, C.J. Kähler, C. Tropea, Comparison of CCD, CMOS and intensified cameras, Exp. Fluids 42 (3) (2007) 403–411, http://dx.doi.org/10.1007/s00348-006-0247-1.

[26] T. Kissel, E. Baum, A. Dreizler, J. Brübach, Two-dimensional thermographic phosphor thermometry using a CMOS high speed camera system, Appl. Phys. B 96 (4) (2009) 731–734, http://dx.doi.org/10.1007/s00340-009-3626-5.

[27] S. Someya, M. Uchida, K. Tominaga, H. Terunuma, Y. Li, K. Okamoto, Lifetime-based phosphor thermometry of an optical engine using a high-speed CMOS camera, Int. J. Heat Mass Transfer 54 (17–18) (2011) 3927–3932, http://dx.doi.org/10.1016/j.ijheatmasstransfer.2011.04.032.